



# Investigation of dioctahedral smectite hydration properties by modeling of X-ray diffraction profiles: Influence of layer charge and charge location

Eric Ferrage, Bruno Lanson, Boris.A. Sakharov, Nicolas Geoffroy, Emmanuel Jacquot, Victor.A. Drits

## ► To cite this version:

Eric Ferrage, Bruno Lanson, Boris.A. Sakharov, Nicolas Geoffroy, Emmanuel Jacquot, et al.. Investigation of dioctahedral smectite hydration properties by modeling of X-ray diffraction profiles: Influence of layer charge and charge location. *American Mineralogist*, Mineralogical Society of America, 2007, 92, pp.1731-1743. <10.2138/am.2007.2273>. <hal-00193677>

**HAL Id: hal-00193677**

**<https://hal.archives-ouvertes.fr/hal-00193677>**

Submitted on 4 Dec 2007

**HAL** is a multi-disciplinary open access archive for the deposit and dissemination of scientific research documents, whether they are published or not. The documents may come from teaching and research institutions in France or abroad, or from public or private research centers.

L'archive ouverte pluridisciplinaire **HAL**, est destinée au dépôt et à la diffusion de documents scientifiques de niveau recherche, publiés ou non, émanant des établissements d'enseignement et de recherche français ou étrangers, des laboratoires publics ou privés.



1 Investigation of dioctahedral smectite hydration properties by modeling of X-ray  
2 diffraction profiles: Influence of layer charge and charge location

3

4

### Revision 3

5

6

7 Eric Ferrage<sup>1,2\*</sup>, Bruno Lanson<sup>1</sup>, Boris A. Sakharov<sup>3</sup>, Nicolas Geoffroy<sup>1</sup>, Emmanuel Jacquot<sup>2</sup>,  
8 and Victor A. Drits<sup>3</sup>

9

10 <sup>1</sup> Environmental Geochemistry Group, LGIT – Maison des Géosciences, Joseph Fourier  
11 University – CNRS, BP53, 38041 Grenoble cedex 9, France

12 <sup>2</sup> ANDRA, Parc de la Croix Blanche, 1-7 rue Jean Monnet, 92298 Châtenay-Malabry  
13 cedex, France

14 <sup>3</sup> Geological Institute, Russian Academy of Sciences, 7 Pyzhevsky street, 109017  
15 Moscow, Russia

16

17 \*Corresponding author: [e.ferrage@nhm.ac.uk](mailto:e.ferrage@nhm.ac.uk) . Present address: The Natural History  
18 Museum, Department of Mineralogy, Cromwell Road, London SW7 5BD, United Kingdom.

## ABSTRACT

19  
20  
21  
22  
23  
24  
25  
26  
27  
28  
29  
30  
31  
32  
33  
34  
35  
36  
37  
38  
39  
40  
41  
42

Hydration of the  $<1\ \mu\text{m}$  size fraction of a high-charge montmorillonite (Clay Minerals Society Source Clay SAz-1), and of low- and high-charge beidellites (Source Clays SbId-1 and SbCa-1, respectively) was studied by modeling of X-ray diffraction patterns recorded under controlled relative humidity (RH) for Sr- and/or Ca-saturated specimens. The influence of layer charge and charge location on smectite hydration was studied. Distribution of layers with different hydration states (dehydrated – 0W, monohydrated – 1W, bi-hydrated – 2W, or tri-hydrated – 3W) within smectite crystals often leads to two distinct contributions to the X-ray diffraction pattern, each contribution having different layer types randomly interstratified. Structure models are more heterogeneous for beidellite than for montmorillonite. For beidellite, two distinct populations of particles with different coherent scattering domain sizes account for the heterogeneity. Increased hydration heterogeneity in beidellite originates also from the presence of 0W (non-expandable) and of 1W layers under high relative humidity (RH) conditions. Similarly, after ethylene-glycol (EG) solvation, some beidellite layers incorporate only one plane of EG molecules whereas homogeneous swelling was observed for montmorillonite with the systematic presence of two planes of EG molecules.

For montmorillonite and beidellite, the increase of layer charge shifts the 2W-to-1W and the 1W-to-0W transitions towards lower RH values. For all samples, layer thickness of 0W, 1W, and 2W layer types was similar to that determined for low-charge SWy-1 montmorillonite (Source Clay SWy-1), and no change of layer thickness was observed as a function of the amount or of the location of layer charge. Layer thickness however increased with increasing RH conditions.

## INTRODUCTION

43  
44  
45  
46  
47  
48  
49  
50  
51  
52  
53  
54  
55  
56  
57  
58  
59  
60  
61  
62  
63

Bentonite, a rock containing mostly smectite, is a promising buffer material for engineered barriers for nuclear waste disposal. This potential results from its mechanical self-healing ability, its low hydraulic conductivity, and its high sorption capacity. This combination is expected to prevent or delay possible radionuclide migration. However, the properties of smectite can be altered by storage-induced conditions such as the thermal pulse resulting from the waste package. By analogy with burial diagenesis of clayey sediments (Weaver 1960; Hower and Mowatt 1966; Burst 1969; Shutov et al. 1969; Perry and Hower 1972; Hower et al. 1976; among many others), smectite is expected to transform to illite by way of intermediate interstratified structures with increasing temperature. This transition was originally conceived as following smectite dehydration (Burst 1969; Shutov et al. 1969; Perry and Hower 1972). More recently, structural changes affecting smectite during the early stages of transformation have been shown to impact essentially the location and amount of layer charge (Sato et al. 1996; Drits et al. 1997; Beaufort et al. 2001), the initial smectite being a low-charge montmorillonite with dominant octahedral charge. Sato et al. (1996) proposed that beidellite-like layers (with dominant tetrahedral charge) initially form from montmorillonite in addition to an increase in layer charge. Then, these beidellite-like layers transform to illite. This proposal is supported by hydrothermal alteration experiments conducted at moderate temperatures (<200°C, see Beaufort et al. 2001) leading to beidellitic layers from alteration of montmorillonite.

64  
65  
66  
67

Modification of layer charge and charge location can possibly affect smectite hydration ability. Crystalline swelling of 2:1 phyllosilicates is controlled indeed by the balance between repulsive forces between adjacent 2:1 layers and attractive forces between hydrated interlayer cations and the negatively charged surface of 2:1 layers (Norrish 1954;

68 Van Olphen 1965; Kittrick 1969a, 1969b; Laird 1996, 1999). Thus crystalline swelling is  
69 characterized by the amount of layer charge and its location (octahedral vs. tetrahedral).  
70 Different hydration states may correspond to 0, 1, 2 or 3 “planes” of H<sub>2</sub>O molecules in  
71 smectite interlayers. Intercalation of H<sub>2</sub>O planes produces a stepwise hydration depending on  
72 RH, easily detected by X-ray diffraction (XRD) by an increase in basal spacing  
73 (Nagelschmidt 1936; Bradley et al. 1937; Mooney et al. 1952; Méring and Glaeser 1954;  
74 Norrish 1954; Walker 1956; among others).

75         From these considerations, an increase in layer charge increases attractive forces  
76 between the hydrated interlayer cation and the 2:1 layers, thus decreasing interlayer thickness.  
77 Charge location may affect smectite hydration from the charge under-saturation of oxygen  
78 atoms defining the basal surfaces of 2:1 layers. In montmorillonite-like layers, the charge  
79 under-saturation resulting from R<sup>2+</sup>-for-R<sup>3+</sup> substitutions in the octahedral sheet is distributed  
80 among a large number of basal oxygen atoms which are thus weakly under-saturated. In  
81 contrast, when Al<sup>3+</sup>-for-Si<sup>4+</sup> substitutions occur in tetrahedral sites the charge deficit is  
82 distributed by the three nearest neighbor basal oxygen atoms. These oxygen atoms are  
83 strongly under-saturated and produce strong attractive interactions with interlayer cations.  
84 This strong local under-saturation is sometimes assumed to decrease layer hydration (e.g.,  
85 Laird 1996, 1999). However, experimental results are not consistent with this expected  
86 influence of the size and location of layer charge on hydration behavior. For example, Sato et  
87 al. (1992) reported similar *d*(001) values for smectite with different layer-charge locations,  
88 and smaller *d*(001) values were not observed for smectite with higher layer charge.  
89 Furthermore, Chiou and Rutherford (1997) and Michot et al. (2005) reported an increase in  
90 H<sub>2</sub>O content with increasing layer charge. Similar results were obtained by Laird (1999) who  
91 attributed the increased hydration to H<sub>2</sub>O adsorption on external surfaces of the crystallites.

92 This article complements Ferrage et al. (2005b), in which the hydration of low-  
93 charge montmorillonite was studied, and investigates the effect of the size and location of  
94 layer charge on smectite hydration. The hydration of three reference smectites, including  
95 high-charge montmorillonite, and low- and high-charge beidellites, is considered as a function  
96 of relative humidity after saturation by  $\text{Ca}^{2+}$  and  $\text{Sr}^{2+}$ .

97

98

## MATERIAL AND METHODS

99

### 100 Sample preparation

101

102 Smectites used here are montmorillonite and beidellite samples from the Source Clay  
103 Repository of The Clay Minerals Society. The high-charge montmorillonite (SAz-1) has a  
104 structural formula of:  $[(\text{Al}_{2.80} \text{Fe}^{3+}_{0.20} \text{Mg}_{1.00})(\text{Si}_{7.86} \text{Al}_{0.14})\text{O}_{20}(\text{OH})_4] \text{M}^{+}_{1.14}$  (Jaynes and  
105 Bigam 1987). Compared to SWy-1 montmorillonite studied by Ferrage et al. (2005b), SAz-1  
106 has more  $\text{Mg}^{2+}$ -for- $\text{Al}^{3+}$  octahedral substitutions and limited tetrahedral substitution.

107 Low-charge SbId-1 beidellite (Glen Silver Pit, DeLamare Mine, Idaho) has a  
108 structural formula of:  $[(\text{Al}_{3.77} \text{Fe}^{3+}_{0.11} \text{Mg}_{0.21})(\text{Si}_{7.27} \text{Al}_{0.73})\text{O}_{20}(\text{OH})_4] \text{M}^{+}_{0.67}$  (Post et al. 1997).

109 High-charge SbCa-1 beidellite contains more  $\text{Al}^{3+}$ -for- $\text{Si}^{4+}$  tetrahedral substitutions with a  
110 structural formula:  $[(\text{Al}_{3.82} \text{Fe}^{3+}_{0.18} \text{Mg}_{0.06})(\text{Si}_{6.80} \text{Al}_{1.20})\text{O}_{20}(\text{OH})_4] \text{M}^{+}_{1.07}$ .

111 For all samples, size fractionation to  $< 1 \mu\text{m}$  was obtained by centrifugation. Then,  
112 ion exchange was achieved with  $1 \text{ mol.L}^{-1}$  aqueous solutions of  $\text{CaCl}_2$ , for SAz-1 only, and  
113  $\text{SrCl}_2$ , with three steps of saturation followed by three washing steps, as described by Ferrage  
114 et al. (2005b). Resulting samples are hereafter referred to as Ca- and Sr-SAz-1, Sr-SbId-1 and  
115 Sr-SbCa-1.

116

## 117 **X-ray diffraction and fitting strategy**

118

119 XRD patterns were recorded from oriented preparations of the air-dried homoionic  
120 samples. Full-width at half-maximum intensity (FWHM) of the 001 reflection and 00*l*  
121 reflection irrationality ( $\xi$  parameter) were measured to qualitatively estimate hydration  
122 heterogeneity (see Ferrage et al. 2005b). The  $\xi$  parameter is calculated as the standard  
123 deviation of the  $l \times d(00l)$  values (in Å) for all measurable 00*l* reflections over the 2-50°2 $\theta$   
124 angular range, although some of these reflections may correspond to various interstratified  
125 structures. These values are listed in Table 1.

126 Models combine the XRD modeling algorithm of Drits and coworkers (Sakharov and  
127 Drits 1973; Drits and Sakharov 1976; Drits et al. 1997; Sakharov et al. 1999) with a trial-and-  
128 error approach to quantify hydration heterogeneity. The calculation of the XRD profile  
129 includes the mean number of layers (N) in the coherent scattering domains (CSDs), the  
130 absorption coefficient ( $\mu^*$ ), and the preferred orientation of the sample ( $\sigma^*$ ). The *z* coordinates  
131 of dehydrated (0W), monohydrated (1W), and bi-hydrated (2W) layers, and crystal strains  
132 ( $\sigma_z$ ) described by Ferrage et al. (2005b) were used. H<sub>2</sub>O molecules were distributed in 2W  
133 smectite as a unique plane of H<sub>2</sub>O molecules on each side of the central interlayer mid-plane,  
134 at ~1.20 Å along the *c*\* axis. The number of interlayer H<sub>2</sub>O molecules in hydrated layers was  
135 considered a variable parameter.

136 The fitting strategy developed by Ferrage et al. (2005b) was used to model XRD  
137 patterns. A main structure, periodic along the *c*\* axis where possible, was used to reproduce  
138 the experimental XRD pattern. If required, additional contributions to the diffracted intensity  
139 were introduced. These additional contributions are related to random interstratifications of  
140 two or three layer types (0W, 1W, 2W layers), which are hereafter referred to as  
141 heterogeneous structures as compared to the main structure. Because RH values were < 80%,



142 tri-hydrated layers (3W layers at 18.0-18.5 Å) were not observed, as transition from 2W-to-  
143 3W smectite occurs for RH values of > 90% for Ca-exchanged smectites (Watanabe and Sato  
144 1988). Up to four structures (periodic and/or interstratified) were used for very heterogeneous  
145 samples but these contributions are not necessarily related to distinct populations of crystals.  
146 To minimize the number of adjustable parameters, layers of same hydration state present in  
147 different structures were assumed to have identical properties. Thus, for a given sample, each  
148 layer type (0W, 1W or 2W layers) was assigned a chemical composition (number of interlayer  
149 H<sub>2</sub>O molecules and cations, and chemical composition of the 2:1 layer), layer thickness, and  
150 atomic coordinates for each component. Similarly, a unique value of  $\sigma^*$  and  $\sigma_z$  parameters  
151 was assigned for each RH value. Each parameter was allowed to vary with RH. For beidellite,  
152 models consider either (1) a unique CSD size for all interstratified structures at a given RH, or  
153 (2) the physical mixture of two or more interstratified structures with different CSD sizes (see  
154 below).

155 Hereafter, indices “00 $l$ ” and “001, 002, ...” are used to identify experimental  
156 diffraction maxima, although these maxima correspond to interstratified and not to periodic  
157 structures.

158

## 159 **RESULTS**

160

### 161 **Qualitative description of experimental patterns**

162

163 **Ca- and Sr-saturated montmorillonite SAz-1.** At 0% RH, Ca-SAz-1 (Fig. 1a)  
164 exhibits a 001 reflection at  $\sim 11.65$  Å, a position intermediate between 0W and 1W smectite,  
165 indicating hydration heterogeneity. Accordingly, the 001 reflection is broad (FWHM =  $1.05^\circ$ ,  
166 Table 1) and a large value of  $\xi$  parameter was obtained ( $0.56$  Å, Table 1). In contrast, the

167 pattern of Sr-SAz-1 recorded at 0% RH (Fig. 1b) is typical of 1W smectite (001 at  $\sim 12.10$  Å)  
168 with a low value of  $\xi$  ( $0.04$  Å), but note the high FWHM of the 001 reflection ( $0.88^\circ$ ). At 20%  
169 RH, the  $d(001)$  value of Sr-SAz-1 at  $\sim 13.1$  Å is intermediate between 2W and 1W smectites.  
170 Experimental diffraction maxima are poorly defined, and peaks at  $\sim 6.1$  Å (002 reflection of  
171 1W smectite), and at  $\sim 5.1$  Å (003 reflection of 2W smectite) are observed (Fig. 1b). For this  
172 sample, high values are obtained for  $\xi$  and FWHM of the 001 reflection ( $1.20$  Å and  $1.66^\circ$ ,  
173 respectively). In contrast, Ca-SAz-1 exhibits a 001 reflection at  $\sim 14.9$  Å and well-defined  
174 diffraction maxima of 2W smectite. Over the 35-80% RH range, XRD patterns for Ca- and  
175 Sr-SAz-1 are similar, and correspond to dominant 2W smectite (Ca:  $d(001) = 15.1$ - $15.6$  Å; Sr:  
176  $d(001) = 15.2$ - $15.9$  Å – Table 1). Note that the 002 reflection is poorly defined whatever the  
177 RH (Figs. 1a, 1b).

178 **Sr-saturated beidellite (SbId-1 and SbCa-1).** XRD patterns of both beidellites  
179 samples include reflections at  $\sim 7.2$  and  $\sim 3.6$  Å (K on Figs. 1c, 1d), produced by a minor  
180 contribution from kaolinite-group minerals. At 0% RH, Sr-SbId-1 displays poorly defined  
181 diffraction maxima with a 001 reflection at  $\sim 11.10$  Å and large values of FWHM and  $\xi$  ( $1.28^\circ$   
182 and  $0.76$  Å, respectively, Fig. 1c, Table 1). In contrast, Sr-SbCa-1 shows well-defined  
183 diffraction maxima corresponding to 1W smectite ( $d(001) \sim 12.0$  Å) and low values for  
184 FWHM of the 001 reflection and  $\xi$  ( $0.75^\circ$  and  $0.04$  Å, respectively). At 20% RH,  $d(001)$   
185 values at  $\sim 12.3$ - $12.4$  Å for both samples indicate a 1W smectite, along with low values for  
186 FWHM and  $\xi$ . At ambient RH, the  $d(001)$  values near  $14.9$  Å for Sr-SbId-1 and near  $15.2$  Å  
187 for Sr-SbCa-1 indicate dominant 2W smectite with well-defined diffraction maxima.  
188 However, both XRD patterns present a high-angle shoulder of the 001 reflection and a peak at  
189  $\sim 6.1$  Å corresponding to 1W smectite (Figs. 1c, 1d), which increases  $\xi$ . From 40 to 80% RH,  
190 the peak at  $\sim 6.1$  Å is absent and the high-angle shoulder of the 001 reflection decreases with  
191 increasing RH (Figs. 1c, 1d). The  $d(001)$  values are similar for the two samples throughout

192 this RH range and low values of FWHM and  $\xi$  systematically indicate the dominance of 2W  
193 smectite. As for SAz-1, the 002 reflection of 2W smectite is poorly defined.

194 Note also the peaks at  $\sim 25$  Å and  $\sim 22$  Å for samples recorded over the 35-80% RH  
195 and 0-20% RH range, respectively. These peaks may be attributed to an ordered interstratified  
196 structure consisting of 2W and 0W and of 1W and 0W smectite, respectively (Figs. 1c, 1d).  
197 For Sr-SbCa-1, these reflections are similar to those reported by Chipera and Bish (2001).

198

### 199 **Modeling of X-ray diffraction profiles**

200

201 Structure models providing optimum fits shown in Figure 1 are described  
202 schematically (relative proportion and composition of each structure) in Figure 2 as a function  
203 of RH. Structural parameters are listed in Table 2.

204 **Ca- and Sr-SAz-1 montmorillonite.** XRD patterns for Ca-SAz-1 and Sr-SAz-1 over  
205 the 0-80% RH range were fitted assuming two structures (Figs. 1a, 1b, 2a, 2b). Over the 20-  
206 80% RH range for Ca-SAz-1 and the 35-80% RH range for Sr-SAz-1, the model consists of a  
207 main structure dominated by 2W smectite and of a second, heterogeneous, structure  
208 containing 0W, 1W, and 2W layers (Figs. 2a, 2b). 2W layers are systematically prevailing in  
209 the heterogeneous structure except for Sr-SAz-1 at 35% RH where 2W and 1W smectite are  
210 present in equal amounts (Figs. 2a, 2b). Relative abundance of the heterogeneous structure  
211 decreases with increasing RH. The proportion of 1W and 0W layers in the dominantly 2W  
212 structure decreases also with increasing RH. Both trends account for the sharpening and the  
213 increased intensity of the reflection at  $\sim 7.75$  Å with increasing RH (Figs. 1a, 1b). At 20% RH,  
214 two contributions were used to fit the pattern of Sr-SAz-1, a near-periodic 1W smectite, and a  
215 heterogeneous structure containing 0W, 1W, and 2W layers. 1W and 2W layers prevail in the  
216 latter structure which accounts for the reflection at  $\sim 5.1$  Å. The different compositions of the

217 two structures produce the broadening of the 001 reflection observed at this RH (1.66°, Table  
218 1). At 0% RH, patterns of Ca-SAz-1 and Sr-SAz-1 were fitted assuming a main structure  
219 dominated by 1W smectite and a more heterogeneous structure dominated by 0W layers  
220 (Figs. 2a, 2b). The irrationality of 00*l* reflections for Ca-SAz-1 ( $\xi = 0.56 \text{ \AA}$ ) is produced by  
221 the high amount of 0W layers in the main structure, in which 1W layers prevail, and by the  
222 strong contribution of the most heterogeneous structure.

223         With increasing RH, the layer thickness of 1W and 2W layers increases for both  
224 samples to accommodate the larger numbers of interlayer H<sub>2</sub>O molecules (Table 2), as  
225 reported by Ferrage et al. (2005b) for low-charge montmorillonite. Among other parameters,  
226  $\sigma^*$  was found nearly constant (6.7-7.5°) for all XRD patterns except for 0% RH, whereas N  
227 and  $\sigma_z$  are steadily decreasing and increasing, respectively, with increasing RH.

228         **Sr-SbId-1 and Sr-SbCa-1 beidellite.** In the optimum structure model determined  
229 for Sr-SbId-1 and Sr-SbCa-1, interstratified structures can have different N values. In this  
230 case, the evolution of beidellite hydration results from the hydration properties of two particle  
231 populations with distinct N values. However, to minimize the number of adjustable  
232 parameters other parameters (layer chemical composition, layer thickness,  $\sigma^*$ ,  $\sigma_z$ , e.g.) are  
233 identical for all layer types, whatever the interstratified structure (Table 2).

234         At 60% and 80% RH, one particle population contains essentially 2W layers and  
235 accounts for the main features of the experimental patterns (Figs. 2c, 2d, 3). The second  
236 population is a very heterogeneous structure of small CSD size (3.5 layers, Table 2, Figs. 2c,  
237 2d, 3), which produces the asymmetry of the 001 reflection at high angles and of the 005  
238 reflection at low angles (Fig. 3). At 40% RH, a second interstratified structure with dominant  
239 2W layers coexisting with 1W layers occurs with a large CSD size (30 and 40% of 1W layers  
240 for Sr-SbId-1 and Sr-SbCa-1, respectively, Figs. 2c, 2d). Structure models determined at 35%  
241 RH include four structures, one structure having a low CSD size (Figs. 2c, 2d). Finally, two

242 structures were considered to reproduce patterns recorded at 20% and 0% RH. The first  
243 structure, with a large CSD size, is dominated by 1W smectite and accounts for the shape of  
244 the 001 reflection and for the position of other maxima. For Sr-SbId-1 at 0% RH, this  
245 structure incorporates significant proportions of 0W layers. The second structure, whose  
246 content does not depend on RH, has smaller CSD size and contains 1W and 0W layers, the  
247 proportion of 0W layers increasing with decreasing RH (Figs. 2c, 2d).

248 For both Sr-SbId-1 and Sr-SbCa-1 the amount of kaolinite-group minerals did not  
249 vary (~16% and ~10% for Sr-SbId-1 and Sr-SbCa-1, respectively, Figs. 2c, 2d). As observed  
250 for montmorillonite (this study and Ferrage et al. 2005b), layer thickness of 1W and 2W  
251 layers increased with increasing RH for Sr-SbId-1 (11.95-12.70 Å and 15.12-15.65 Å,  
252 respectively) and for Sr-SbCa-1 (11.98-12.70 Å and 15.10-15.60 Å, respectively). Among  
253 other parameters,  $\sigma^*$  is nearly constant (7.0-8.0° and 4.8-5.5° for Sr-SbId-1 and Sr-SbCa-1,  
254 respectively). With increasing RH,  $\sigma_z$  increases whereas N decreases, except at 0% RH for Sr-  
255 SbId-1.

256 For beidellite, the low intensity reflection at ~25 Å over the 35-80% RH range may  
257 correspond to an ordered (Reichweit parameter  $R = 1$  with maximum possible degree of  
258 order, R1-MPDO, see Drits and Tchoubar 1990) interstratified structure containing similar  
259 proportions of 0W and 2W layers (Figs. 1c, 1d, 5). Similarly, the reflection at ~22 Å observed  
260 over the 0-20% RH range may correspond to a R1-MPDO structure containing 1W and 0W  
261 layers in similar proportions. These features are discussed below.

262 Note that fits of similar quality were obtained for Sr-SbId-1 and Sr-SbCa-1 with  
263 structures models in which all contributions contain identical layers and have identical crystal  
264 parameters (N,  $\sigma^*$ ). However, modeling of XRD patterns obtained after ethylene-glycol (EG)  
265 solvation allows rejection of these alternative models (see below).

266            **Modeling of X-ray diffraction profiles after EG solvation.** XRD patterns obtained  
267 after EG solvation of Ca-saturated SWy-1 and SAz-1 and of Sr-saturated SbId-1 and SbCa-1  
268 are compared to calculated profiles in Figure 4 and optimal structural parameters are listed in  
269 Table 3. For montmorillonite, the best model involves a unique structure of 2EG layers (with  
270 two planes of interlayer EG molecules), interstratified with non-expandable (0EG) layers at  
271 1% and 2% in Ca-SWy-1 and Ca-SAz-1, respectively. These contents of collapsed layers are  
272 similar to samples at 80% RH. No 1EG layers were found.

273            XRD patterns of EG-solvated beidellite were only simulated assuming two  
274 interstratified structures (Table 3). One (with a large CSD size) contains mostly 2EG layers,  
275 and the second is more heterogeneous and contains 15% of 1EG and 15% of 0EG layers.  
276 After EG solvation, the relative abundance of the most heterogeneous structure (with a low  
277 CSD size) is similar to that of the population with a low CSD size in the air-dried state (38%  
278 and 42% for Sr-SbId-1 and Sr-SbCa-1, respectively). This similarity strongly supports the  
279 presence of different particle populations. Combining the two contributions leads to a  
280 2EG:1EG:0EG ratio of 86:7:7 for both Sr-SbId-1 and Sr-SbCa-1.

281

282            **DISCUSSION**

283

284            **Structure models**

285

286            **Montmorillonite.** Structure models determined for SAz-1 (this study) and SWy-1  
287 (Ferrage et al. 2005b) are consistent for a given interlayer cation. From ambient to 80% RH  
288 these models include two interstratified structures dominated by 2W layers, one being more  
289 heterogeneous with the presence of the three layer types (0W, 1W and 2W layers – Figs. 2a,

290 2b). Hydration of high-charge SAz-1 montmorillonite is thus homogeneous, with a slight  
291 segregation of 2W layers.

292 **Beidellite.** Complex structure models with numerous contributions were required to  
293 reproduce experimental XRD patterns for beidellites. At ambient RH, the large high-angle  
294 asymmetry of the 001 reflection and reflections from both 1W- and 2W-dominated structures  
295 required a greater number of contributions. In addition, structure models include a  
296 heterogeneous structure containing high proportions of 0W and 1W layers even at 80% RH.  
297 This contribution has a small CSD size (3.5-5.0 layers), and its relative proportion is constant  
298 (~40-45% for Sr-SbId-1 and Sr-SbCa-1) through the RH range investigated.

299 The particle population with a large CSD size (population A in Figure 6) exhibits  
300 transitions to higher hydration states with increasing RH: from 0W/1W to 1W and further to  
301 2W (for Sr-SbId-1) and from 1W to 2W (for Sr-SbCa-1). In both samples, the 1W-2W  
302 transition occurs through intermediate 2W/1W interstratified structures. The particle  
303 population with a small CSD size (population B in Figure 6) maintains its heterogeneous layer  
304 composition throughout the RH range despite the steady increase of the 2W layer proportion,  
305 at the expense of 0W layers, with increasing RH.

306 **Impurities in beidellites.** For Sr-SbId-1 and Sr-SbCa-1, low-intensity reflections  
307 occur at  $\sim 25$  Å and  $\sim 22$  Å (for the 35-80% and 0-20% RH ranges, respectively). The  $\sim 25$  Å  
308 peak possibly corresponds to a R1-MPDO structure containing similar proportions of 0W and  
309 2W layers (Figs. 1c, 1d). Similarly, the reflection at  $\sim 22$  Å possibly corresponds to a R1-  
310 MPDO structure containing 1W and 0W layers in similar proportions. The positions of these  
311 reflections do not significantly change after EG solvation (Fig. 4). The relative proportion of  
312 this structure was determined for Sr-SbId at 80% RH (Fig. 5). For Figure 5a, the optimum  
313 model (Fig. 2c) is shown for  $2\theta < 5^\circ$ . Note that the computed “background” intensity is  
314 inconsistent with the measured one. Over this region, a R1-MPDO structure containing 0W

315 and 2W layers exhibits two main reflections at  $\sim 25.0$  Å and  $\sim 12.5$  Å, the latter being much  
316 weaker. To reproduce the shoulder at  $\sim 25$  Å, the R1-MPDO structure should contribute  $\sim 3\%$   
317 of the total diffracted intensity (Fig. 5b), without affecting the relative proportion of the  
318 different layer types. Consequently, the low-angle reflections may be related to impurities.

319 **Origin of hydration heterogeneity in beidellite.** Two populations of particles were  
320 found in beidellites (Fig. 6). Hydration of population A, with a large CSD size, is  
321 homogeneous with dominant 1W and 2W layer types except for Sr-SbId-1 at 0 and 35% RH  
322 and for Sr-SbCa-1 at 35 and 40% RH. In contrast, hydration of population B, with a small  
323 CSD size, is heterogeneous over the entire RH range for each beidellite. This observation  
324 suggests that layer charge and charge location in population B are likely similar for both  
325 samples. In addition, populations A and B probably differ in both samples from the  
326 heterogeneity of their layer charge distributions.

327 Because of population B, the number of 0W and 1W layers is relatively high at 80%  
328 RH for Sr-SbId-1 (14% and 10%, respectively) and Sr-SbCa-1 (9% and 14%, respectively). In  
329 contrast, at this high RH value, Sr-SWy-1 contains 2% of 0W and 1W layers and Sr-SAz-1  
330 shows 1% and 4% of 0W and 1W layers, respectively. Hydration heterogeneity persists at  
331 high relative humidity only for beidellite. XRD profile modeling of EG-solvated samples  
332 confirmed the observed hydration/swelling heterogeneity of beidellite (global 2EG:1EG:0EG  
333 ratio of 86:7:7 for both Sr-SbId-1 and Sr-SbCa-1), although EG solvation is known to induce  
334 homogeneous configuration of smectite interlayers (2EG layers). Collapsed layers after EG  
335 solvation are considered as non-expandable layers. Although the nature of 1EG layers is  
336 unknown, they may possess a higher layer charge than smectite (vermiculite-type layers).  
337 Note that 0EG and 1EG layers are present mostly in the most heterogeneous structure.  
338 Finally, 2EG layers in populations A and B probably have a similar layer charge, which is



339 close to that determined for the whole sample [ $\sim 0.67$  and  $\sim 1.07$  per  $O_{20}(OH)_4$ , respectively for  
340 SbId-1 and SbCa-1] because of the high proportion of 2EG layers in EG-solvated samples.

341 The near complete swelling of layers following EG solvation is observed for  
342 montmorillonite and for population A of beidellite. In contrast, for beidellite increasing layer  
343 charge from the mean layer charge may produce vermiculite-like layers, discrete illite layers  
344 or irreversibly collapsed K-beidellite layers when potassium is present as assumed for SbId-1  
345 (Post et al. 1997). However, heterogeneous structures where layers have different  
346 hydration/swelling abilities is not *a priori* characteristic of smectite with layer charge  
347 originating in the tetrahedra, although such interstratified structures probably occur more  
348 frequently in beidellite compared to montmorillonite. Further study is required to assess the  
349 systematic (?) presence of highly heterogeneous structures in natural beidellite.

350

### 351 **Influence of layer charge and charge location on hydration of 2:1 phyllosilicates**

352 The influence of layer charge on smectite hydration (Fig. 7) was derived from the  
353 relative proportions of layer types as a function of RH. For all samples, XRD patterns were  
354 recorded from RH = 35 (ambient) to 80% RH in adsorption conditions and then at 20% and  
355 0% RH in desorption conditions. Relative proportions of the different layer types were  
356 considered for montmorillonite and beidellite along the adsorption (40%, 60% and 80% RH)  
357 and desorption (35%, 20% and 0% RH) pathways. See Ferrage et al. (2005b) for data on Ca-  
358 and Sr-saturated SWy-1 montmorillonite.

359 **Smectite.** 0W layer content is equal or slightly lower for Ca-SAz-1 compared to Ca-  
360 SWy-1 and gradually decreases with increasing RH (Fig. 7a). In adsorption conditions, 2W  
361 layers dominate the two samples, 1W layers being more abundant for Ca-SWy-1. At 20% RH  
362 along the desorption pathway, Ca-SAz-1 is dominated by 2W layers ( $\sim 75\%$ ) whereas Ca-  
363 SWy-1 contains similar amounts of 2W and 1W layers. This difference indicates that the 2W-

364 to-1W transition occurs at lower RH values for Ca-SAz-1 compared to Ca-SWy-1. At 0% RH,  
365 the two samples have similar contents of 2W and 1W layers, 0W layers being more abundant  
366 in Ca-SAz-1.

367 The proportion of 0W layers is similar in Sr-SAz-1 and Sr-SWy-1 (Fig. 7b) except at  
368 0% RH, where Sr-SAz-1 is dominated by 1W layers and Sr-SWy-1 is mostly dehydrated. At  
369 20% RH, Sr-SWy-1 and Sr-SAz-1 are dominated by 1W layers, with a greater number of 0W  
370 and 2W layers in the latter. At 35% RH, 2W layers prevail in Sr-SAz-1 and Sr-SWy-1 is  
371 mostly monohydrated. These observations are similar to those made on Ca-saturated  
372 specimens: 2W-to-1W and 1W-to-0W transitions are shifted towards lower RH values with  
373 increasing layer charge. Along the adsorption pathway, the number of 2W layers in Sr-SAz-1  
374 is similar (at 40 and 80% RH) or slightly lower (at 60% RH) compared to Sr-SWy-1, in  
375 contrast to Ca-saturated samples.

376 Proportions of layer types are plotted in Figures 7c, 7d as a function of RH for  
377 beidellite. Figure 7c describes the overall behavior of the two populations of particles, and the  
378 behavior of population A is given in Figure 7d. Note that for population A, the layer charge is  
379 likely homogeneous and close to that of the entire sample. Along the adsorption pathway and  
380 at 20% RH, hydration of Sr-SbCa-1 and Sr-SbId-1 is similar for the entire sample and for  
381 population A crystallites (Figs. 7c, 7d). At 35% RH, Sr-SbCa-1 contains more 2W layers than  
382 Sr-SbId-1 indicating that a greater layer charge shifts the 2W-to-1W transition to lower RH  
383 values, similar to montmorillonite. At 0% RH, the different composition of the two samples  
384 produces a shift of the 1W-to-0W transition to lower RH values with increasing layer charge.

385 Hydration of montmorillonite and beidellite is compared in Figures 7e, 7f for a given  
386 layer charge [ $\sim 0.7$  per  $O_{20}(OH)_4$  for SWy-1 and SbId-1, and  $\sim 1.1$  per  $O_{20}(OH)_4$  for SAz-1 and  
387 SbCa-1]. Hydration of SbCa-1 and SbId-1 may be estimated from their population A. For a  
388 similar layer charge, hydration is greater for beidellite than for montmorillonite over 0-80%

389 RH. Additional studies on beidellite with a more homogenous layer charge distribution are  
390 required to confirm this observation.

391 **Expandable 2:1 phyllosilicates.** In summary, it appears that a greater layer charge  
392 increases the stability of 1W and 2W layers towards lower RH values, at least upon H<sub>2</sub>O  
393 desorption, for montmorillonite and beidellite. This trend probably occurs owing to the  
394 greater number of interlayer cations when increasing layer charge. Whatever the size and  
395 location of layer charge, smectite interlayer thickness and the number of interlayer H<sub>2</sub>O  
396 molecules are about constant for a given interlayer cation and RH value (see below). As the  
397 number of interlayer H<sub>2</sub>O molecules is systematically higher than necessary to provide  
398 octahedral coordination to interlayer cations, the hydration sphere of a given cation is constant  
399 for smectite. The amount of H<sub>2</sub>O molecules coordinating interlayer cations thus increases at  
400 the expense of H<sub>2</sub>O molecules not directly bound to these cations when layer charge  
401 increases. As the 2W-to-1W transition occurs as interlayer H<sub>2</sub>O molecules not coordinated to  
402 interlayer cations are still present in 2W smectite (Ferrage et al. 2007) the higher density of  
403 hydrated interlayer cations is likely responsible for the observed increased stability of most  
404 hydrated layers towards lower RH values when layer charge is increased.

405 Although consistent with the molecular simulations performed by Smith et al.(2004),  
406 this increased stability may appear as contradicting the conventional wisdom that high-charge  
407 layers are less hydrated than low-charge layers (Laird 1999). The inverse relationship between  
408 hydration (as measured from layer basal distance) and layer charge is the foundation to  
409 differentiate smectite from vermiculite (Brindley 1980; Calle and Suquet 1988; Suquet and  
410 Pezerat 1988). In addition, trioctahedral vermiculite basal distance decreases with increasing  
411 layer charge (Calle and Suquet 1988; Suquet and Pezerat 1988), and the stability of less  
412 hydrated layers is increased towards higher RH values when layer charge is increased (Suquet  
413 and Pezerat 1987). The present results can be reconciled with the hydration behaviors

414 attributed to smectite and vermiculite. In the present study, stability of hydrated smectite  
415 layers increases with increasing layer charge and is thus maximum at the upper limit of  
416 smectite layer charge [0.5-0.6 net charge per  $O_{10}(OH)_2$ ]. This charge threshold is the lower  
417 charge limit for vermiculite, whose hydration differs from that of smectite most likely because  
418 of the prevalence of attractive forces between interlayer cations and the 2:1 layer above this  
419 threshold. The total number of interlayer  $H_2O$  molecules is however slightly higher for  
420 vermiculite (6.6-7.6 per  $O_{20}(OH)_4$  – Le Renard and Mamy 1971; Calle et al. 1977; Slade et al.  
421 1985) than for smectite (5.0-7.0 per  $O_{20}(OH)_4$  – This study and Laird 1999; Ferrage et al.  
422 2005b). The reduced layer basal distance is thus not due to a reduced hydration of vermiculite  
423 compared to smectite but more likely linked to the reorganization of  $H_2O$  molecules  
424 coordinated to interlayer cations. Consistently, increasing the layer charge favors ordering in  
425 the interlayer cation distribution (Drits 1987), and the layer-charge boundary between  
426 smectite and vermiculite may correspond to the onset of this ordering. This boundary may  
427 also coincide with the formation of a two-dimensional network of  $H_2O$  molecules in the  
428 interlayer above a certain density of  $H_2O$  molecules bound to interlayer cations. This  
429 hypothesis is supported by the reduced breadth of the  $H_2O$  molecule distributions determined  
430 for saponite when layer charge is increased (Ferrage et al. 2005a).

431 In addition, the contrast of layer basal distance observed between dioctahedral  
432 smectite (this study) and trioctahedral vermiculite (Suquet and Pezerat 1987; Calle and Suquet  
433 1988; Suquet and Pezerat 1988) is possibly enhanced by the ordered distribution of  
434 isomorphic substitutions in vermiculite, which probably favors interlayer species ordering.  
435 Trioctahedral vermiculites are indeed isostructural to trioctahedral micas from which they  
436 differ essentially by the hydrophilic character of their interlayer cations. Layer stacking,  
437 which is commonly ordered for trioctahedral vermiculite in contrast to dioctahedral smectite,  
438 and more especially to montmorillonite, can also favor ordering of interlayer species and thus

439 enhance the observed contrast of layer basal distance. The influence of charge location  
440 (tetrahedral vs. octahedral) is probably minor, at least for dioctahedral smectite, because  
441 montmorillonite and beidellite display an equal hydration behavior as a function of layer  
442 charge (Fig. 7). Finally, note that 3W layer appears not to follow the same trend, in that their  
443 stability is more restricted when layer charge of dioctahedral smectite is increased (Laird et al.  
444 1995). However, in this study layer-charge increase may be influenced by the relative  
445 proportion of tetrahedral substitutions.

446         **Interlayer thickness (IT).** The ratio of IT to cation radius is plotted in Figure 8 as a  
447 function of RH. Similar values were obtained for all samples, in agreement with Sato et al.  
448 (1992) who reported similar  $d(001)$ -values for hydrated smectite regardless of the size and  
449 location of layer charge. This observation is consistent with the similar H<sub>2</sub>O content  
450 determined at a given RH for each sample (Table 2) but is counter to the frequently assumed  
451 decrease of layer thickness with increasing layer charge (Laird 1996).

452         For Ca-saturated samples, the greater number of 2W layers and the associated  
453 increase of H<sub>2</sub>O content in SAz-1 compared to SWy-1 (Figs. 7a, 7b) is consistent with the  
454 water-adsorption isotherms reported by Chiou and Rutherford (1997) for the same samples.  
455 By comparing the water-adsorption isotherms for SAz-1 and SWy-1, these authors showed  
456 that the interlayer H<sub>2</sub>O uptake increases with the layer charge. Laird (1999) criticized these  
457 results as counter to the frequently accepted decrease of hydration ability with an increase in  
458 smectite layer charge. However, Laird (1999) reported similar  $d(001)$  values for smectites  
459 with different charges and attributed the increased number of adsorbed H<sub>2</sub>O to the adsorption  
460 on clay external surfaces. The results in the present article account only for interlayer H<sub>2</sub>O  
461 and support the conclusions of Chiou and Rutherford (1997), in agreement with Michot et al.  
462 (2005). The water-vapor adsorption isotherms obtained by the latter authors on synthetic

463 saponite showed an increased number of adsorbed H<sub>2</sub>O molecules with increasing layer  
464 charge over the entire RH range.

465

#### 466 **Dehydrated layer thickness**

467

468           Except for Sr-SbId-1 at 0% RH, the thickness of 0W layers was equal to 10.0 Å for  
469 Ca- and Sr-SAz-1 and for Sr-saturated beidellite (Table 2). Similar results were obtained for  
470 SWy-1 when saturated with Mg<sup>2+</sup>, Ca<sup>2+</sup> and Sr<sup>2+</sup>, whereas the thickness of 0W layers was  
471 lower for samples saturated with monovalent cations at 9.6 Å, 9.6 Å and 10.0 Å for Na<sup>+</sup>, Li<sup>+</sup>  
472 and K<sup>+</sup>, respectively (Ferrage et al. 2005b). The latter values are consistent with those  
473 expected for dehydrated specimens. Because of the smaller radii of divalent cations, layer  
474 thickness values of ~10.0 Å appear high. Ferrage et al. (2005b) observed an increase of  $\sigma_z$  in  
475 samples dominated by 2W layers compared to those dominated by 1W layers. This increase  
476 was attributed to the greater interlayer thickness, and thus to the weaker electrostatic  
477 interactions between the 2:1 layer and interlayer cations in 2W layers. Similar results were  
478 obtained for SAz-1 and beidellite samples (Table 2). However,  $\sigma_z$  does not decrease further in  
479 0W layers, except for Na-SWy-1 at 0% RH (Ferrage et al. 2005b), probably because of  
480 residual H<sub>2</sub>O in the “dehydrated” layers. Monovalent interlayer cations ensures a local  
481 compensation of under-saturated basal oxygen atoms, whereas charge compensation is more  
482 diffuse with long-distance interactions, possibly through H-bonds, for divalent cations. The  
483 latter configuration would probably favor the presence of H<sub>2</sub>O molecules linked with under-  
484 saturated oxygen atoms via H-bonds. The presence of additional H<sub>2</sub>O molecules is favored  
485 also by the higher ionic potential (valency/ionic radius) of divalent cations. The coulombic  
486 radius of a H<sub>2</sub>O molecule ( $r = 1.4\text{-}1.5$  Å – Williams et al. 1994; Li and Nussinov 1998) is  
487 similar to that of a K<sup>+</sup> cation ( $r = 1.38$  Å – Shannon 1976), and their presence may account for

488 the 10.0 Å layer thickness determined here and by Ferrage et al. (2005b) for 0W layers in  
489 samples saturated with divalent cations. Residual H<sub>2</sub>O molecules would produce an increased  
490  $\sigma_z$ , as observed, because of the different radii of H<sub>2</sub>O molecules and interlayer cations. Local  
491 charge compensation by monovalent interlayer cations reduces the number of interlayer H<sub>2</sub>O  
492 molecules, as observed for K- and Na-saturated SWy-1 montmorillonites (Ferrage et al.  
493 2005b). For these two samples, the thickness of 0W layers is similar to that expected for  
494 totally dehydrated layers at 9.6 Å and 10.0 Å for Na- and K-saturated SWy-1 at 0% RH,  
495 respectively (Ferrage et al. 2005b). For Li-saturated SWy-1 montmorillonite, the layer  
496 thickness is higher than expected and  $\sigma_z$  is higher at 0% compared to other RH conditions,  
497 possibly from the presence of residual H<sub>2</sub>O molecules in 0W layers, in agreement with the  
498 high affinity of Li<sup>+</sup> for H<sub>2</sub>O.

499

#### 500 **Limitations for qualitative indicators of smectite hydration heterogeneity**

501

502 For SWy-1, Ferrage et al. (2005b) related smectite-hydration heterogeneity to the  
503 qualitative  $\xi$  parameter describing the irrationality of 00 $l$  reflection positions. Values of  $\xi$   
504 were < 0.4 Å when a specific layer type accounted for > 70% of the layer content. However,  
505 this relation is mostly due to the specific distribution of the different layer types in SWy-1.  
506 The different layer types are indeed randomly distributed in SWy-1, with possibly a slight  
507 tendency to segregation. In this case, diffraction features follow Méring's principle (Méring  
508 1949) and an increased heterogeneity broadens the 001 reflection and increases the positional  
509 irrationality of 00 $l$  reflections.

510 The relative proportion of the prevailing layer type is plotted in Figure 9 as a  
511 function of  $\xi$  for SAz-1, SbId-1 and Sr-SbCa-1. For beidellite, results are given after  
512 subtraction of the kaolinite contribution and normalization of the smectite layer abundances to

513 100%. As reported by Ferrage et al. (2005b), for most samples,  $\xi$  is  $> 0.4 \text{ \AA}$  when the  
514 dominant layer type accounts for  $\sim 70\%$  or less of the layer content. However, note the  
515 “outliers” in Figure 9. For instance, Sr-SbId-1 and Sr-SbCa-1 at 40% RH do not follow the  
516 trend and most beidellites have low  $\xi$  values relative to their hydration heterogeneity (Figs.  
517 2c, 2d, 9). Furthermore, Sr-SbCa-1 at 35% and 40% RH have similar contents of the  
518 dominant layer type of 55-59% of 2W layers (Fig. 9) but different  $\xi$  of  $1.54 \text{ \AA}$  and  $0.05 \text{ \AA}$  at  
519 35% and 40% RH, respectively (Table 1). Similarly, Sr-SAz-1 contains 66 % of 1W layers at  
520 20% RH and 69% of 2W layers at 35% RH but has different  $\xi$  values of  $1.20 \text{ \AA}$  and  $0.12 \text{ \AA}$ ,  
521 respectively (Table 1).

522         These discrepancies are related to the inability of qualitative parameters, such as  $\xi$ , to  
523 describe hydration heterogeneity in complex systems. The  $\xi$  parameter depends not only on  
524 the proportion of layer types but also on their distribution within crystallites. Similarly, the  
525 FWHM of the 001 reflection is influenced by CSD size and hydration heterogeneity. Some  
526 discrepancies observed for beidellite are explained from the experimental XRD patterns (Figs.  
527 1c, 1d). At 40% RH, the 001 reflection of Sr-SbId-1 and Sr-SbCa-1 exhibits a sharp  
528 maximum and a pronounced high-angle shoulder. This shoulder corresponds to a  
529 heterogeneous structure with a small CSD size (Figs. 2c, 2d), which does not contribute much  
530 intensity to the XRD pattern. In contrast, the essentially 2W structure contributes more to the  
531 001 reflection (position and shape) and most of the diffraction features, including  $\xi$ . Similarly,  
532 the FWHM of the 001 reflection is not influenced by the high-angle shoulders, although they  
533 stem from hydration heterogeneity (Figs. 1c, 1d, 2c, 2d).

534         The high value of  $\xi$  for Sr-SbCa-1 at 35% RH results mainly from the reflection at  
535  $\sim 6.1 \text{ \AA}$ , which results from an interstratified structure dominated by 1W layers in a sample  
536 dominated by 2W layers. However, this structure accounts for 8% of the clay fraction and  
537 does not modify significantly the proportion of the different layer types compared to the same



538 sample at 40% RH. The inability of the qualitative parameters, such as  $\xi$ , to provide a realistic  
539 description of the beidellite hydration is a result of the segregation of the different layer types,  
540 leading to the numerous structures involved in the models and their compositions.

541 Finally, Sr-SAz-1 recorded at 20% and 35% RH have nearly equal contents of 1W  
542 and 2W layers, respectively, but different  $\xi$  values. For each sample, structure models consist  
543 of a main interstratified structure, dominated by 1W layers at 20% RH and 2W layers at 35%  
544 RH, whereas a minor, more heterogeneous structure contains 1W and 2W layers in nearly  
545 equal proportions. The different values of  $\xi$  obtained for these two samples (Fig. 9) result  
546 from the different structure factors for 1W and 2W layers. The structure factor is larger for  
547 2W layers than for 1W layers over the low-angle region, and if they exist equally in an  
548 interstratified structure, then related reflections are near the position expected for a periodic  
549 2W smectite (e.g., peak at  $\sim 5.1$  Å for Sr-SAz-1 at 20% RH, see Fig. 1b). The coexistence of a  
550 1W/2W interstratified structure with a near periodic 2W smectite does not produce significant  
551 peak shift or broadening, and low value of  $\xi$  is determined at 35% RH. In contrast, the  
552 coexistence of a 1W/2W interstratified structure with a near periodic 1W structure produces a  
553 greater  $\xi$  value, as measured at 20% RH.

554 The above discussion outlines the limitations of qualitative parameters to describe  
555 hydration heterogeneity. These criteria are relevant only when layer types are randomly  
556 distributed (Ferrage et al. 2005b). Relevance of the qualitative parameters may be enhanced  
557 by careful analysis of position, intensity and profile of basal reflections over the entire 2-  
558  $50^\circ 2\theta$  CuK $\alpha$  angular range. However, quantitative analysis of smectite hydration as obtained  
559 from XRD pattern modeling is preferred if the distribution of layer types is to be determined.

560

561

## ACKNOWLEDGMENTS

562

563           This paper is a result of a PhD thesis granted by Andra (French National Agency for  
564 Nuclear Waste Disposal). Andra is thanked for permission to publish this manuscript and for  
565 financial support. BL acknowledges financial support from the CNRS/PICS709 program, and  
566 from the CNRS/SdU “postes rouges” fellowships granted to BAS. VAD and BAS are grateful  
567 to the Russian Science Foundation for financial support. We thank Laurent Michot (LEM,  
568 Nancy, France) for the fruitful discussions about smectite hydration, and John Yang (Univ.  
569 Missouri) for providing the structural formula of SbCa-1. The manuscript was much  
570 improved by the constructive reviews of Javier Cuadros and David Laird, and by the editorial  
571 assistance of AE Steve Guggenheim.

572  
573  
574  
575  
576  
577  
578  
579  
580  
581  
582  
583  
584  
585  
586  
587  
588  
589  
590  
591  
592  
593  
594  
595

## REFERENCES

- Beaufort, D., Berger, G., Lacharpagne, J.-C., and Meunier, A. (2001) An experimental alteration of montmorillonite to a di + trioctahedral smectite assemblage at 100 and 200°C. *Clay Minerals*, 36, 211-225.
- Bradley, W.F., Grim, R.E., and Clark, G.F. (1937) A study of the behavior of montmorillonite upon wetting. *Zeitschrift Kristallographie*, 97, 216-222.
- Brindley, G.W. (1980) Order-disorder in clay mineral structures. In G.W. Brindley, and G. Brown, Eds., *Crystal Structures of Clay Minerals and their X-ray Identification*, p. 125-195. Mineralogical Society, London.
- Burst, J.F. (1969) Diagenesis of Gulf Coast clayey sediments and its possible relation to petroleum migration. *American Association of Petroleum Geologists Bulletin*, 53, 73-93.
- Calle, C. de la, Pezerat, H., and Gasperin, M. (1977) Problèmes d'ordre-désordre dans les vermiculites - Structure du minéral calcique hydraté à deux couches. *Journal de physique*, 38, C7 128-133.
- Calle, C. de la and Suquet, H. (1988) Vermiculite. In S.W. Bailey, Ed., *Hydrous phyllosilicates (exclusive of micas)*, 19, p. 455-496. Mineralogical Society of America, Chantilly, Va.
- Chiou, C.T. and Rutherford, W. (1997) Effects of exchanged cation and layer charge on the sorption of water and egme vapors on montmorillonite clays. *Clays & Clay Minerals*, 45, 867-880.
- Chipera, S.J. and Bish, D.L. (2001) Baseline studies of the clay minerals society source clays: Powder X-ray diffraction analyses. *Clays & Clay Minerals*, 49, 398-409.

596 Drits, V.A. (1987) Electron diffraction and high-resolution electron microscopy of mineral  
597 structures, 304 p. Springer Verlag, Berlin Heidelberg.

598 Drits, V.A., Lindgreen, H., Sakharov, B.A., and Salyn, A.S. (1997) Sequential structure  
599 transformation of illite-smectite-vermiculite during diagenesis of Upper Jurassic  
600 shales, North Sea. *Clay Minerals*, 33, 351-371.

601 Drits, V.A. and Sakharov, B.A. (1976) X-Ray structure analysis of mixed-layer minerals, 256  
602 p. Dokl. Akad. Nauk SSSR, Moscow.

603 Drits, V.A. and Tchoubar, C. (1990) X-ray diffraction by disordered lamellar structures:  
604 Theory and applications to microdivided silicates and carbons, 371 p. Springer-  
605 Verlag, Berlin.

606 Ferrage, E., Kirk, C.A., Cressey, G., and Cuadros, J. (2007) Dehydration of Ca-  
607 montmorillonite at the crystal scale. Part 1. Structure evolution. *American*  
608 *Mineralogist*, in press.

609 Ferrage, E., Lanson, B., Malikova, N., Plançon, A., Sakharov, B.A., and Drits, V.A. (2005a)  
610 New insights on the distribution of interlayer water in bi-hydrated smectite from X-ray  
611 diffraction profile modeling of 00*l* reflections. *Chemistry of Materials*, 17, 3499-3512.

612 Ferrage, E., Lanson, B., Sakharov, B.A., and Drits, V.A. (2005b) Investigation of smectite  
613 hydration properties by modeling of X-ray diffraction profiles. Part 1. Montmorillonite  
614 hydration properties. *American Mineralogist*, 90, 1358-1374.

615 Hower, J., Eslinger, E.V., Hower, M.E., and Perry, E.A. (1976) Mechanism of burial  
616 metamorphism of argillaceous sediments: 1. Mineralogical and chemical evidence.  
617 *Geological Society of America Bulletin*, 87, 725-737.

618 Hower, J. and Mowatt, T.C. (1966) The mineralogy of illites and mixed-layer  
619 illite/montmorillonites. *American Mineralogist*, 51, 825-854.

620 Jaynes, W.F. and Bigham, J.M. (1987) Charge reduction, octahedral charge, and lithium  
621 retention in heated, Li-saturated smectites. *Clays & Clay Minerals*, 35, 440-448.

622 Kittrick, J.A. (1969a) Interlayer forces in montmorillonite and vermiculite. *Soil Science*  
623 *Society of America Journal*, 33, 217-222.

624 ———. (1969b) Quantitative evaluation of the strong-force model for expansion and  
625 contraction of vermiculite. *Soil Science Society of America Journal*, 33, 222-225.

626 Laird, D.A. (1996) Model for crystalline swelling of 2:1 phyllosilicates. *Clays & Clay*  
627 *Minerals*, 44, 553-559.

628 ———. (1999) Layer charge influences on the hydration of expandable 2:1 phyllosilicates.  
629 *Clays & Clay Minerals*, 47, 630-636.

630 Laird, D.A., Shang, C., and Thompson, M.L. (1995) Hysteresis in crystalline swelling of  
631 smectites. *Journal of Colloid and Interface Science*, 171, 240-245.

632 Le Renard, J. and Mamy, J. (1971) Etude de la structure des phases hydratées des phlogopites  
633 altérées par des projections de fourier monodimensionnelles. *Bulletin du Groupe*  
634 *Français des Argiles*, 23, 119-127.

635 Li, A.-J. and Nussinov, R. (1998) A set of van der Waals and Coulombic radii of protein  
636 atoms for molecular and solvent-accessible surface calculation, packing evaluation,  
637 and docking. *Proteins: Structure, function, and genetics*, 32, 111-127.

638 Méring, J. (1949) L'interférence des rayons-X dans les systèmes à stratification désordonnée.  
639 *Acta Crystallographica*, 2, 371-377.

640 Méring, J. and Glaeser, R. (1954) Sur le rôle de la valence des cations échangeables dans la  
641 montmorillonite. *Bulletin de la Société Française de Minéralogie et Cristallographie*,  
642 77, 519-530.

643 Michot, L.J., Bihannic, I., Pelletier, M., Rinnert, E., and Robert, J.L. (2005) Hydration and  
644 swelling of synthetic Na-saponites: influence of layer charge. *American Mineralogist*,  
645 90, 166-172.

646 Mooney, R.W., Keenan, A.G., and Wood, L.A. (1952) Adsorption of water by  
647 montmorillonite. II. Effect of exchangeable ions and lattice swelling as measured by  
648 X-ray diffraction. *Journal of American Chemical Society*, 74, 1371-1374.

649 Nagelschmidt, G. (1936) On the lattice shrinkage and structure of montmorillonite. *Zeitschrift*  
650 *Kristallographie*, 93, 481-487.

651 Norrish, K. (1954) The swelling of montmorillonite. *Discussions of the Faraday society*, 18,  
652 120-133.

653 Perry, E.A. and Hower, J. (1972) Late-stage dehydration in deeply buried pelitic sediments.  
654 *American Association of Petroleum Geologists Bulletin*, 56, 2013-2021.

655 Post, J.L., Cupp, B.L., and Madsen, F.T. (1997) Beidellite and associated clays from the  
656 DeLamar mine and Florida Mountain area, Idaho. *Clays & Clay Minerals*, 45, 240-  
657 250.

658 Sakharov, B.A. and Drits, V.A. (1973) Mixed-layer kaolinite-montmorillonite: a comparison  
659 observed and calculated diffraction patterns. *Clays & Clay Minerals*, 21, 15-17.

660 Sakharov, B.A., Lindgreen, H., Salyn, A., and Drits, V.A. (1999) Determination of illite-  
661 smectite structures using multispecimen X-Ray diffraction profile fitting. *Clays &*  
662 *Clay Minerals*, 47, 555-566.

663 Sato, T., Murakami, T., and Watanabe, T. (1996) Change in layer charge of smectites and  
664 smectite layers in illite/smectite during diagenetic alteration. *Clays & Clay Minerals*,  
665 44, 460-469.

666 Sato, T., Watanabe, T., and Otsuka, R. (1992) Effects of layer charge, charge location, and  
667 energy change on expansion properties of dioctahedral smectites. *Clays & Clay*  
668 *Minerals*, 40, 103-113.

669 Shannon, R.D. (1976) Revised effective ionic radii and systematic studies of interatomic  
670 distances in halides and chalcogenides. *Acta Crystallographica*, A 32, 751-767.

671 Shutov, V.D., Drits, V.A., and Sakharov, B.A. (1969) On the mechanism of a  
672 postsedimentary transformation of montmorillonite into hydromica. In L. Heller, Ed.  
673 *International Clay Conference*, 1, p. 523-531. Israel University Press, Jerusalem,  
674 Tokyo, Japan.

675 Slade, P.G., Stone, P.A., and Radoslovitch, E.W. (1985) Interlayer structures of the two-layer  
676 hydrates of Na- and Ca-vermiculites. *Clays & Clay Minerals*, 33, 51-61.

677 Smith, D.E., Wang, Y., and Whitley, H.D. (2004) Molecular simulations of hydration and  
678 swelling in clay minerals. *Fluid Phase Equilibria*, 222-223, 189-194.

679 Suquet, H. and Pezerat, H. (1987) Parameters influencing layer stacking types in saponite and  
680 vermiculite: A review. *Clays & Clay Minerals*, 35, 353-362.

681 ———. (1988) Comments on the classification of trioctahedral 2:1 phyllosilicates. *Clays and*  
682 *Clay Minerals*, 36, 184-186.

683 Van Olphen, H. (1965) Thermodynamics of interlayer adsorption of water in clays. *Journal of*  
684 *Colloid Science*, 20, 822-837.

685 Walker, G.F. (1956) The mechanism of dehydration of Mg-vermiculite. *Clays & Clay*  
686 *Minerals*, 4, 101-115.

687 Watanabe, T. and Sato, T. (1988) Expansion characteristics of montmorillonite and saponite  
688 under various relative humidity conditions. *Clay Science*, 7, 129-138.

689 Weaver, C.E. (1960) Possible uses of clay minerals in search for oil. *American Association of*  
690 *Petroleum Geologists Bulletin*, 44, 1505-1518.

691 Williams, M.A., Goodfellow, J.M., and Thornton, J.M. (1994) Buried water and internal  
692 cavities in monomeric proteins. *Protein Science*, 3, 1224-1235.



693 **FIGURE CAPTIONS**

694

695 **Figure 1.** Comparison between experimental and calculated XRD patterns as a function of  
696 RH. Experimental and calculated optimal XRD patterns are shown as crosses and as  
697 solid lines, respectively. **a)** Ca-SAz-1. **b)** Sr-SAz-1. **c)** Sr-SbId-1. **d)** Sr-SbCa-1. For  
698 all samples, the gray bar indicates a modified scale factor for the high-angle region.

699

700 **Figure 2.** Structure models obtained from XRD profiles modeling as a function of RH.  
701 Relative proportions, expressed in wt%, of the interstratified contributions are plotted  
702 on the y-axis whereas their compositions (relative proportions of the different layer  
703 types) are plotted on the x-axis. Light gray, dark gray and solid bars represent 0W,  
704 1W, and 2W layers, respectively. Open bars with a dashed outline represent a  
705 kaolinite contribution.

706

707 **Figure 3.** Illustration of the contributions to the calculated profiles for Sr-SbId-1 at 80% RH.  
708 Intensities in the high-angle region ( $10-50^{\circ}2\theta$ ) are scaled by  $\times 10$  compared to the  
709 low-angle region ( $4-10^{\circ}2\theta$ ). Maxima corresponding to kaolinite-group minerals are  
710 labeled Kaol.

711

712 **Figure 4.** Comparison between calculated and experimental XRD patterns obtained after  
713 ethylene-glycol solvation of the samples. Experimental and calculated optimal XRD  
714 patterns are shown as crosses and as solid lines, respectively. For all samples, the  
715 gray bar indicates a modified scale factor for the high-angle region.

716

717 **Figure 5.** Contribution of an ordered R1-MPDO (see text for details) interstratified structure  
718 to the XRD pattern of Sr-SbId-1 recorded at 80% RH. **a)** Experimental and  
719 calculated pattern as in Figure 1c. XRD profile corresponding to the R1-MPDO  
720 structure is shown as open circles. **b)** Optimal fit to the experimental data including  
721 the contribution of a R1-MPDO structure to the diffracted intensity (see text for  
722 details). The gray bar indicates a modified scale factor for the high-angle region.

723

724 **Figure 6.** Evolution of relative abundance of the layer types as function of RH for each  
725 population of particles, including all interstratified structures contributing to that  
726 population, considered for beidellites. **a)** Sr-SbId-1. **b)** Sr-SbCa-1. Triangles,  
727 diamonds, and squares represent 0W, 1W and 2W layers.

728

729 **Figure 7.** Evolution of relative abundance of layer types as a function of RH. **a)** Ca-SAz-1  
730 and Ca-SWy-1. **b)** Sr-SAz-1 and Sr-SWy-1. **c)** Sr-SbId-1 and Sr-SbCa-1. **d)**  
731 Population A of Sr-SbId-1 and Sr-SbCa-1. **e)** Sr-SAz-1 and population A of Sr-  
732 SbCa-1. **f)** Sr-SWy-1 and population A of Sr-SbId-1. Triangles, diamonds, and  
733 squares represent 0W, 1W and 2W layers. Data for Ca- and Sr-SWy-1 are those  
734 reported by Ferrage et al. (2005b). XRD data collection was performed in adsorption  
735 conditions at 40, 60, and 80% RH, and in desorption conditions at 0, 20, 35% RH.

736

737 **Figure 8.** Evolution of layer thickness of hydrated layers as a function of RH for all samples  
738 including SWy-1 (Ferrage et al. 2005b). Interlayer thickness (IT) is represented by  
739 the ratio IT:ionic radius. IT is calculated as the basal distance  $d(001)$  minus the  
740 thickness of the 2:1 layer (6.54 Å). Linear regression lines are plotted for each cation  
741 and include all samples saturated with this cation.

742

743 **Figure 9.** Relative proportion of the major layer type derived from XRD profile modeling as a

744 function of departure from rationality parameter  $\xi$ . Values of these two parameters

745 (70% and 0.4 Å, respectively) limiting the “homogeneous” hydration are shown as

746 dotted lines. Open symbols indicate samples with  $\xi$  parameters  $> 0.4$  Å.

747

## TABLES

**Table 1:** Basal-reflection qualitative parameters (position, width and rationality) as a function of relative humidity.

Sample	Ca-Saz-1			Sr-Saz-1		
	$d(001)$	FWHM	$\xi/X_i$	$d(001)$	FWHM	$\xi/X_i$
~0% (vacuum)	11.65	1.05	0.56/4	12.10	0.88	0.04/4
20%	14.88	0.90	0.13/4	13.15	1.66	1.20/4
~35% (room)	15.10	0.83	0.15/4	15.20	0.92	0.12/4
40%	15.28	0.79	0.12/4	15.33	0.86	0.10/4
60%	15.37	0.74	0.10/4	15.59	0.81	0.25/4
80%	15.62	0.77	0.19/4	15.87	0.80	0.26/4

Sample	Sr-Sbld-1			Sr-SbCa-1		
	$d(001)$	FWHM	$\xi/X_i$	$d(001)$	FWHM	$\xi/X_i$
~0% (vacuum)	11.10	1.28	0.76/4	11.97	0.75	0.04/4
20%	12.34	0.65	0.04/4	12.36	0.80	0.04/4
~35% (room)	14.90	1.23	1.50/4	15.22	0.95	1.54/3
40%	15.29	0.68	0.06/3	15.29	0.87	0.05/3
60%	15.55	0.63	0.05/3	15.55	0.73	0.02/3
80%	15.73	0.61	0.08/3	15.74	0.72	0.11/3

*Notes:* Position [ $d(001)$ ] and FWHM of the 001 reflection are given in Å and in  $^{\circ}2\theta$  Cu  $K\alpha$ , respectively. The  $\xi$  parameter which accounts for the departure from rationality of the 00 $l$  reflection series is calculated as the standard deviation of the  $l \times d(00l)$  values (in Å) for the  $X_i$  measurable reflections over the 2-50 $^{\circ}2\theta$  Cu  $K\alpha$  angular range.

**Table 2:** Optimum structural parameters used for the simulation of XRD profiles.

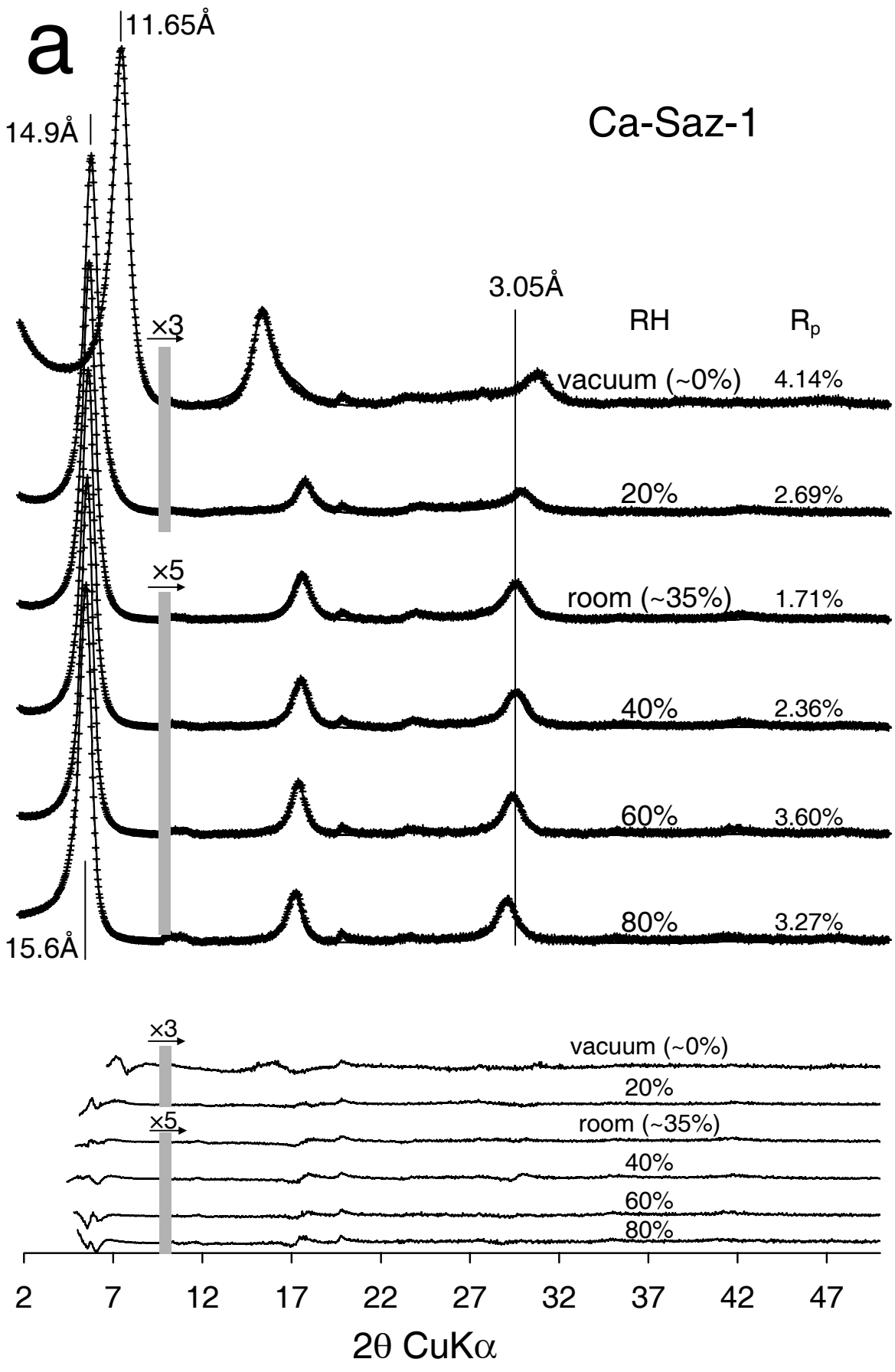
RH	0	20	room	40	60	80
Ca-SAz-1						
L. Tck. 2W	14.30	14.88	15.10	15.16	15.25	15.42
nH <sub>2</sub> O	2*3.1	2*3.2	2*3.2	2*3.3	2*3.5	2*3.5
L. Tck. 1W	11.7	12.61	12.70	12.76	12.80	12.85
nH <sub>2</sub> O	1.5	2.9	3.2	3.2	3.6	4.0
L. Tck. 0W	10.00	10.00	10.00	10.00	10.00	10.00
N	6.1	5.7	5.3	5.2	5.2	4.7
$\sigma^*$	5.0	6.7	7.5	7.5	7.5	7.5
$\sigma_z$	0.25	0.35	0.35	0.35	0.35	0.35
Sr-Saz-1						
L. Tck. 2W	-	15.10	15.26	15.30	15.50	15.65
nH <sub>2</sub> O	-	2*3.0	2*3.0	2*3.0	2*3.1	2*3.5
L. Tck. 1W	12.03	12.30	12.32	12.32	12.40	12.75
nH <sub>2</sub> O	0.3	2.7	3.0	3.0	4.2	4.5
L. Tck. 0W	10.00	10.00	10.00	10.00	10.00	10.00
N	6.3	6.0	5.8	5.8	5.5	4.8
$\sigma^*$	5.0	7.0	7.0	7.0	7.0	7.0
$\sigma_z$	0.20	0.30	0.40	0.40	0.40	0.40
Sr-Sbld-1						
L. Tck. 2W	-	15.12	15.24	15.30	15.50	15.65
nH <sub>2</sub> O	-	2*2.5	2*3.2	2*3.2	2*3.2	2*3.5
L. Tck. 1W	11.95	12.32	12.32	12.32	12.40	12.70
nH <sub>2</sub> O	1.0	2.9	3.5	3.5	3.6	4.5
L. Tck. 0W	9.80	10.00	10.00	10.00	10.00	10.00
N	6.5(5.0)	9.0(4.0)	7.2(3.5)	7.2(3.5)	7.0(3.5)	6.5(3.5)
$\sigma^*$	8.0	7.0	7.0	7.0	7.0	7.0
$\sigma_z$	0.20	0.20	0.25	0.28	0.35	0.30
Sr-SbCa-1						
L. Tck. 2W	-	15.10	15.30	15.30	15.53	15.60
nH <sub>2</sub> O	-	2*3.0	2*3.0	2*3.0	2*3.0	2*3.2
L. Tck. 1W	11.98	12.30	12.30	12.35	12.42	12.70
nH <sub>2</sub> O	1.5	2.5	3.2	3.0	3.0	4.5
L. Tck. 0W	10.00	10.00	10.00	10.00	10.00	10.00
N	7.6(5.0)	6.5(4.0)	6.5(3.5)	6.5(3.5)	6.3(3.5)	5.7(3.5)
$\sigma^*$	4.8	5.2	5.7	5.7	5.7	5.5
$\sigma_z$	0.30	0.25	0.30	0.35	0.35	0.35

*Notes:* Layer thickness (L. Tck.) of 2W, 1W and 0W layers are given in Å. For hydrated layers, the number of interlayer H<sub>2</sub>O molecules (nH<sub>2</sub>O) is indicated per O<sub>20</sub>(OH)<sub>4</sub>. N is the mean number of layers in the coherent scattering domains, orientation parameter ( $\sigma^*$ ) and layer thickness variability parameter ( $\sigma_z$ ) are given in ° and in Å, respectively. N values in parentheses correspond to the second population of particles (see text for details).

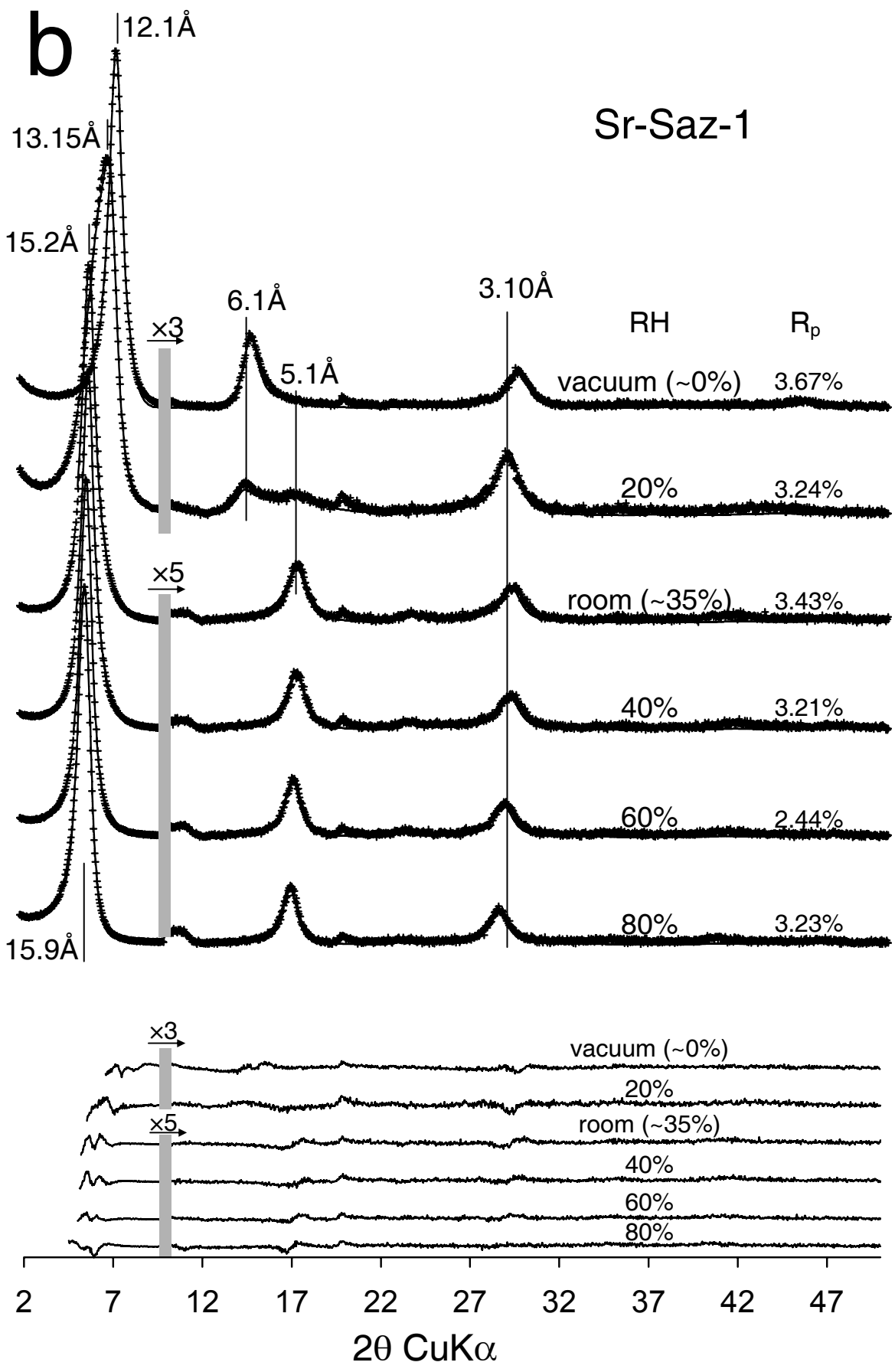
**Table 3.** Optimum structural parameters used for the simulation of XRD profiles obtained after EG solvation.

Sample	S cont. (%)	% 2EG	% 1EG	% 0EG	N	L. Tck. 2EG	L. Tck. 1EG	L. Tck. 0EG	$\sigma^*$	$\sigma_z$
Ca-SWy-1 EG	100	99	0	1	7.0	16.90	-	10.00	8.0	0.27
Ca-SAz-1 EG	100	98	0	2	5.5	16.75	-	10.00	9.0	0.30
Sr-Sbld-1 EG	46	98	0	2	7.2	16.88	12.90	10.00	5.0	0.35
	38	70	15	15	3.8					
Sr-SbCa-1 EG	49	100	0	0	6.8	16.88	12.90	10.00	7.0	0.35
	42	70	15	15	3.8					

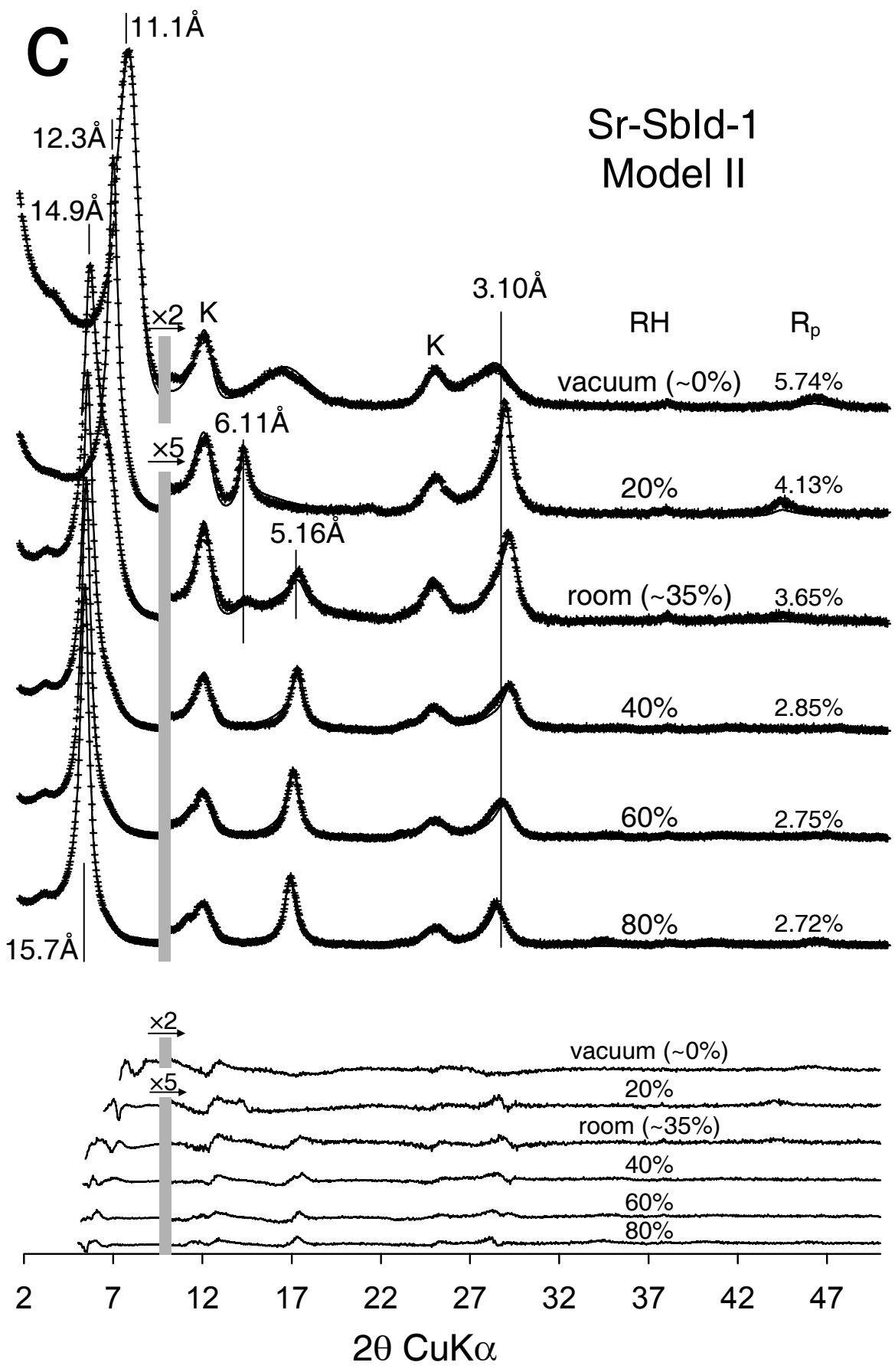
*Notes:* Calculated XRD patterns include the contributions of one or two interstratified structures (S). Layer thickness (L. Tck.) of 2EG, 1EG, and 0EG layers are given in Å. N,  $\sigma^*$ , and  $\sigma_z$  as in Table 2. For beidellites the contribution of kaolinite-group minerals should be added to fit the experimental XRD pattern.

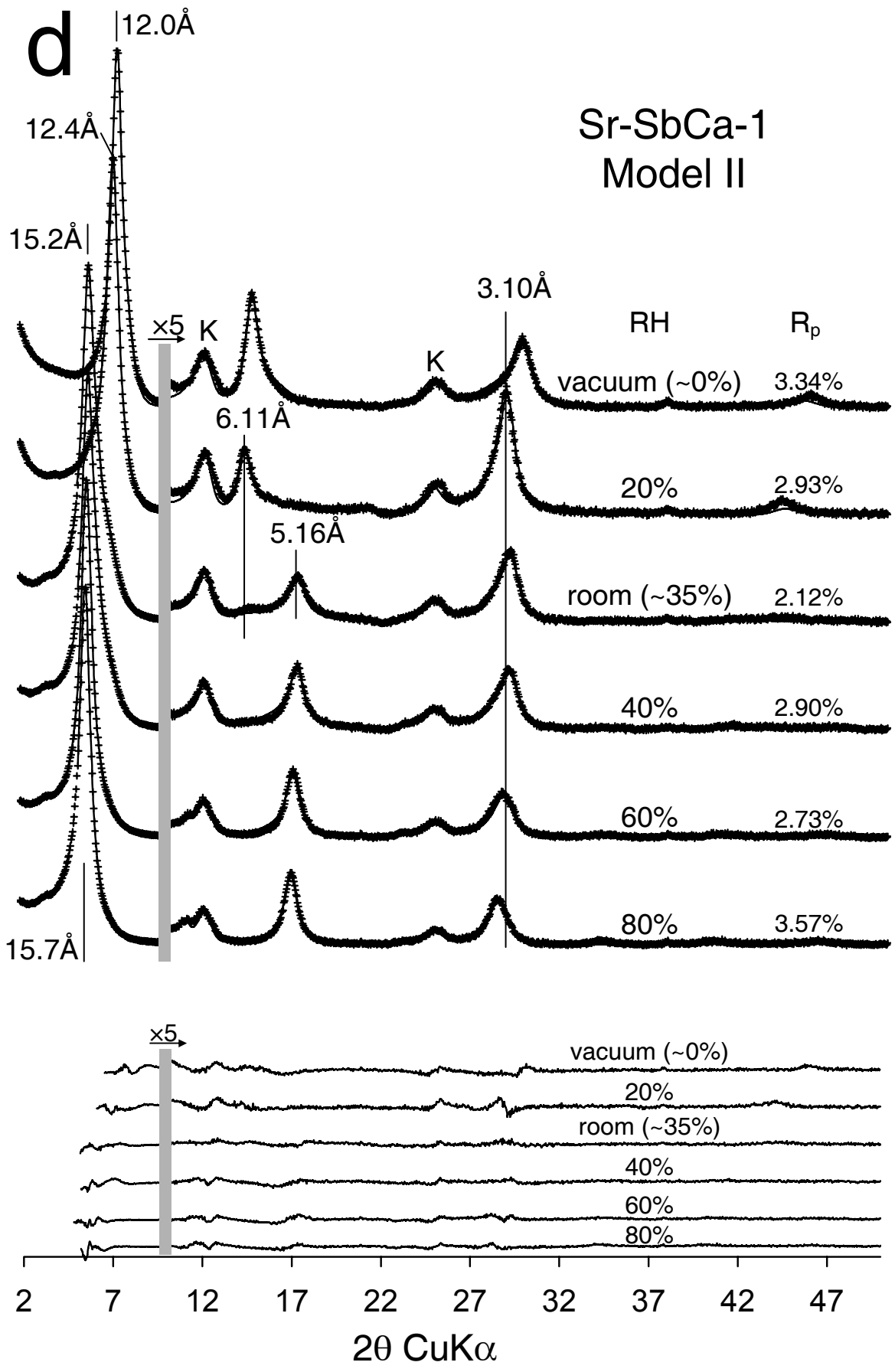


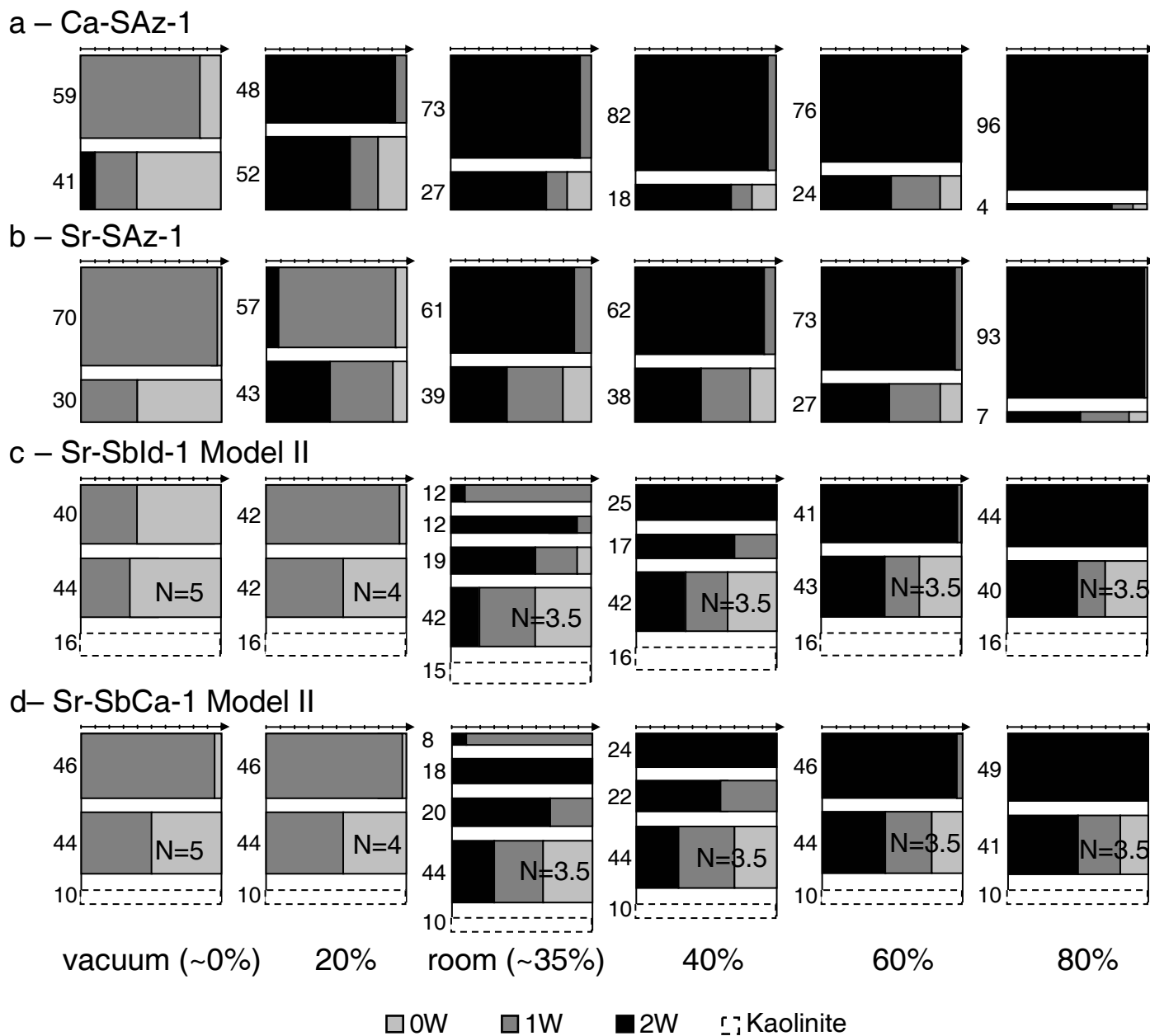
Ms#2273R2 Fig.01

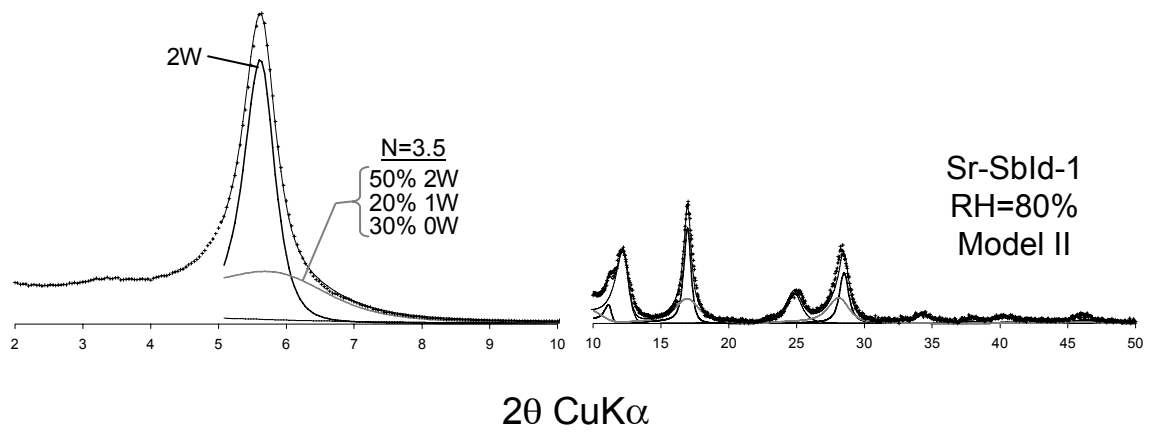


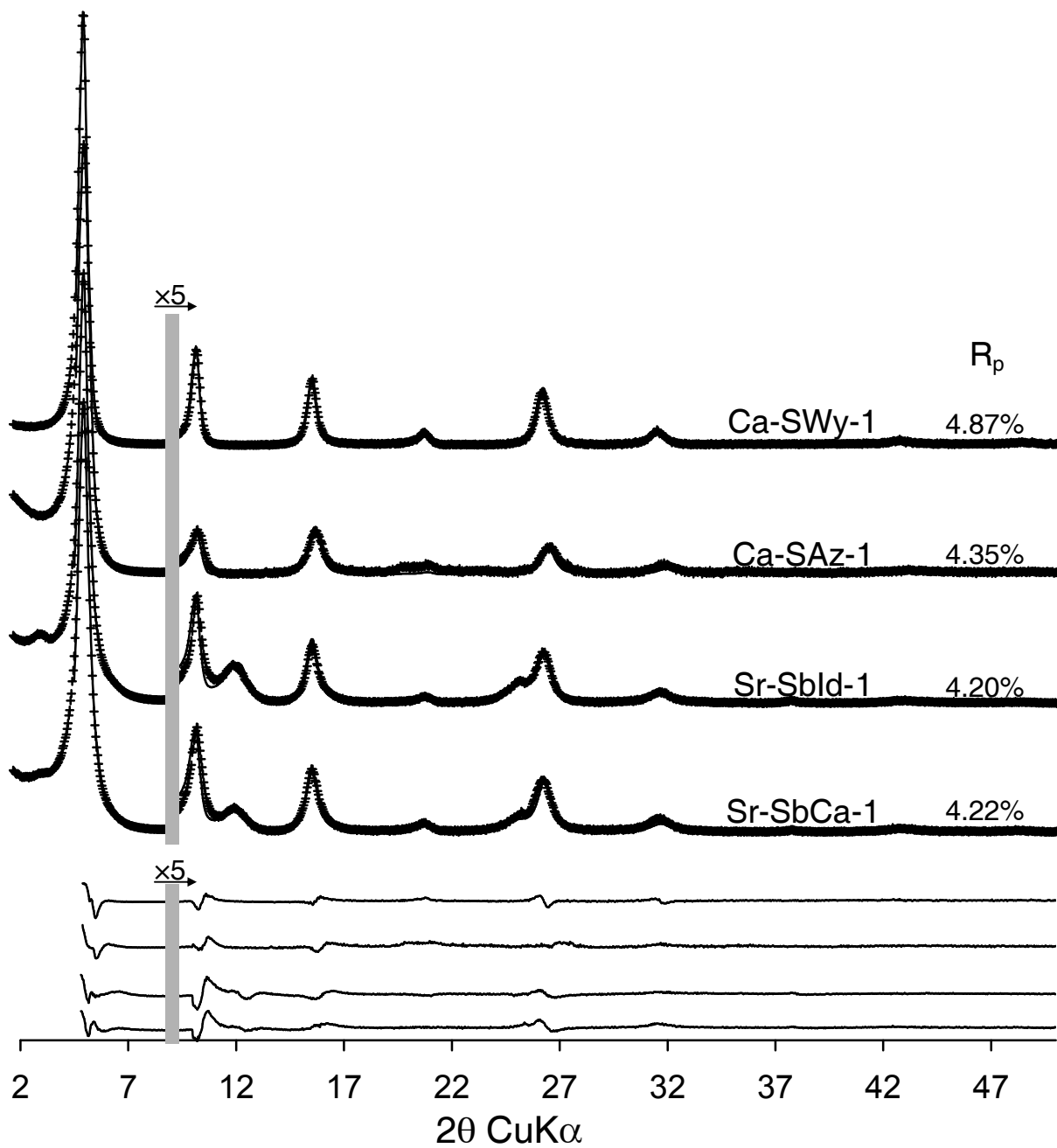


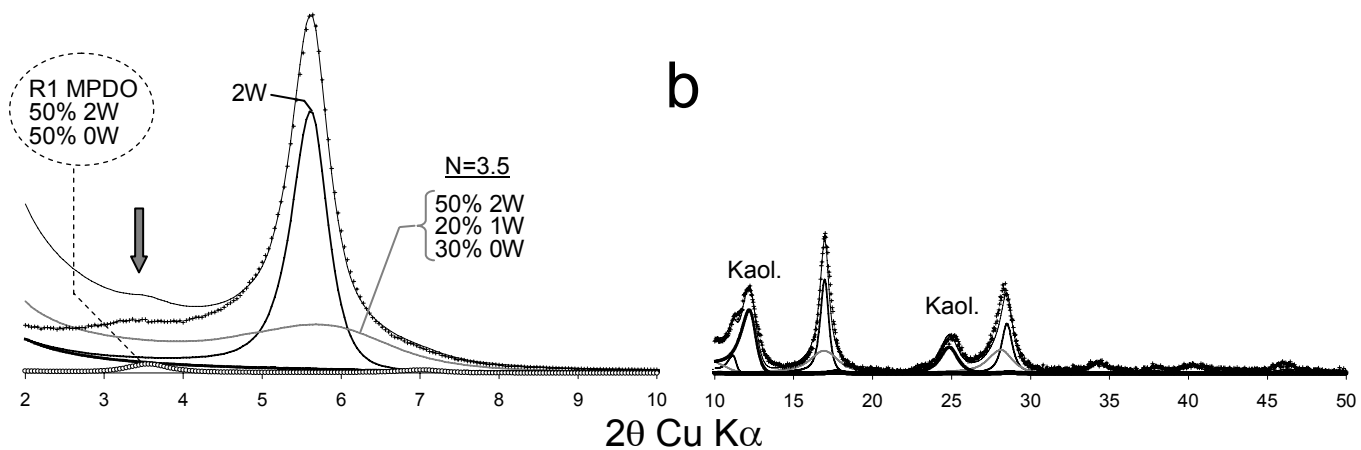
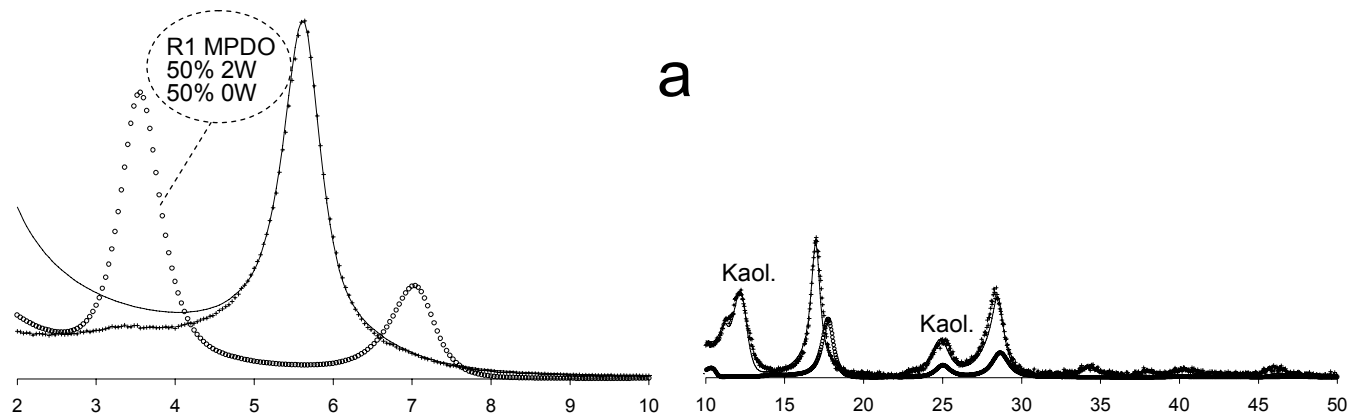


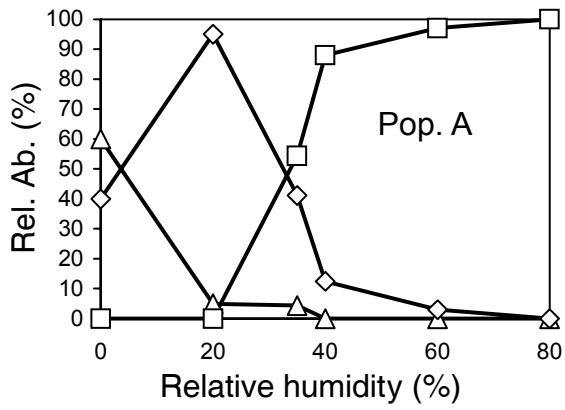




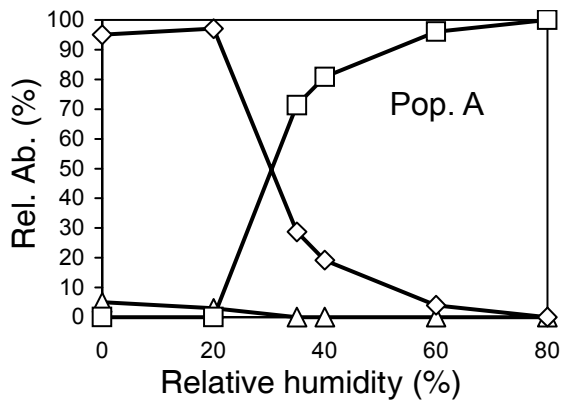
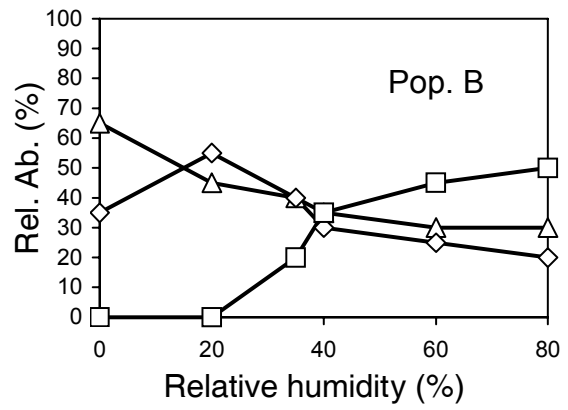








**a**



**b**

